SOFT ROBOTS

A pipeline inspection robot for navigating tubular environments in the sub-centimeter scale

Chao Tang[1,2,3], Boyuan Du[1,2,3], Songwen Jiang[1,2,3], Qi Shao[1,2,3], Xuguang Dong[1,2,3], Xin-Jun Liu[1,2,3], Huichan Zhao[1,2,3]*

In complex systems like aircraft engines and oil refinery machines, pipeline inspection is an essential task for ensuring safety. Here, we proposed a type of smart material–driven pipeline inspection robot (weight, 2.2 grams; length, 47 millimeters; diameter, <10 millimeters) that could fit into pipes with sub-centimeter diameters and different curvatures. We adopted high–power density, long-life dielectric elastomer actuators as artificial muscles and smart composite microstructure–based, high-efficiency anchoring units as transmissions. Fast assembling of components using magnets with an adjustable number of units was used to fit varying pipeline geometries. We analyzed the dynamic characteristics of the robots by considering soft material's unique properties like viscoelasticity and dynamic vibrations and tuned the activation voltage's frequency and phase accordingly. Powered by tethered cables from outside the pipe, our peristaltic pipeline robot achieved rapid motions horizontally and vertically (horizontal: 1.19 body lengths per second, vertical: 1.08 body lengths per second) in a subcentimeter-sized pipe (diameter, 9.8 millimeters). Besides, it was capable of moving in pipes with varying geometries (diameter-changing pipe, L-shaped pipe, S-shaped pipe, or spiral-shaped pipe), filled media (air or oil), and materials (glass, metal, or carbon fiber). To demonstrate its capability for pipeline inspection, we installed a miniature camera on its front and controlled the robot manually from outside. The robot successfully finished an inspection task at different speeds.

INTRODUCTION

In complex systems like aircraft engines and oil refinery machines, there is a large number of pipelines for transmitting water, gases, and oils, usually with various diameters (from a few millimeters to tens of centimeters), changing curvatures (from straight to turning sharply), and covering long distances (from a few centimeters to hundreds of meters). To ensure that they are in a good working order, these pipelines need to be inspected regularly, from both the outside and the inside. Various inspection robots have been developed to navigate pipelines; several of them include wheel-type (*1*), walking-type (*2*), and crawler-type robots (*3*) and other locomotion mechanisms (*4*); adopt electromagnetic motors and gear transmission systems; and are suitable for inspecting pipelines with large diameters. When it comes to small-scale pipelines with diameters of less than a centimeter, the dimensions of robots with such mechanisms of navigation are difficult to scale down.

Bioinspired soft robots using smart materials—such as dielectric elastomer actuators (DEAs) (*5*, *6*), fluidic elastomer actuators (*7*–*9*), hydrogels (*10*), shape memory alloys (SMAs) (*11*, *12*), liquid crystal elastomers (*13*), and magnetic actuators (*14*, *15*)—for actuation exhibit unique advantages for pipeline locomotion. Smart actuating materials have higher power/energy density compared with electromagnetic motors in small volumes and thus are more likely to be scaled to small dimensions (*16*–*18*). Soft robots made of low-moduli materials (for instance, Young's moduli similar to those of soft biological materials) (*19*) can passively adapt to the changing dimensions and shapes of the pipes due to their high degree of freedom and inherently soft bodies. For the task of pipeline inspection, the tubular environment can be challenging depending on whether the pipeline is curved, enclosed, or filled with media. Thus, it requires reliable interactions between the robot and the pipe walls. Designing a soft robot to achieve both agile navigation and effective inspection, especially in small-scale pipes, remains a challenge.

One of the challenges comes from the selection of the actuation method because the navigational performance of soft robots largely depends on the property of their actuators. Pneumatically actuated soft robots designed for pipeline inspection are usually based on an inchworm-type locomotion mechanism, which is easy to seal and miniaturize, as it does not require complex wheels, legs, or other protrusions. However, pneumatic actuators rely on the mass transfer of pressurized air for actuation, and thus the speed would be greatly slowed for long-distance pipe inspection. Compared with pneumatic actuators, DEAs rely on the transfer of charges for actuation, thus are of much faster response and higher power density, and have been widely used in small mobile robots (*20*–*22*). Recent studies (*20*, *23*) also show that the self-clearing of defects in DEAs, based on the carbon nanotubes (CNTs) electrodes, can prolong their service life to million cycles and render the robots with the capability of recovering from external collisions, thus counterbalancing the fact that soft robots actuated by DEAs are prone to breakdown failures, to a certain extent. The inherent compliance, high power density, robustness to damages, and long longevity contribute to the great potential of DEAs as the choice for small-scale pipeline inspection robots.

Another challenge is the design and manufacturing of the robot's navigational mechanism to achieve efficient locomotion in small-scale pipes. Compared with mollusks, mammals have evolved bone structure for rigid support, muscles for soft actuation, and ligaments as a structural form of flexible transmission, which greatly improve their athletic capacity. In soft robot design, the introduction of rigid components can also substantially improve its motion performance like force/motion transmission and load bearing (*24*). Smart composite microstructure (SCM) technology has been widely used in the structural design of microrobots (*25*–*27*), overcoming the limitations

[1]Department of Mechanical Engineering, Tsinghua University, Beijing 100084, China. [2]State Key Laboratory of Tribology, Beijing 100084, China. [3]Beijing Key Lab of Precision/Ultra-Precision Manufacturing Equipment and Control, Beijing 100084, China. *Corresponding author. Email: zhaohuichan@mail.tsinghua.edu.cn

of micromechanical machining techniques. Considering pipeline inspection robots' requirements, SCM technology would be an ideal choice (*28*, *29*) for designing and manufacturing the force/motion transmissions for a small yet efficiently moving robot.

In this work, inspired by the peristaltic motion of earthworms, we proposed a type of pipeline inspection robot that can navigate in pipes with a sub-centimeter diameter and varying curvatures (Fig. 1). We adopted high–power density DEAs as the pipeline robot's elongation unit and SCM-based, high-efficiency transmissions as the anchoring units. By modeling and analyzing the dynamic characteristics of the robots and tuning the robot's activation voltages' frequencies and phases, our peristaltic pipeline robot achieved bidirectional, horizontal, and vertical rapid motion (>1 body length/s) in a subcentimeter-sized pipe, powered by tethered cables from outside the pipe. Besides, it was capable of moving in diameter-changing pipes, L-shaped pipes, S-shaped pipes, spiral-shaped pipes, pipes filled with oils, and pipes made of different materials. We demonstrated its capability for pipeline inspection by installing a miniature camera on its front and controlling the robot to finish a real-time image-recording task in a metal pipeline at different speeds.

RESULTS

Design and assembly of the pipeline robot

The design of our pipeline robot was inspired by the locomotion of an earthworm. It is composed of three segments: front anchoring unit, body elongation unit, and rear anchoring unit, as illustrated in Fig. 1A. The anchoring units and the elongation units contain voltage-driven DEAs for generating the motion of anchoring and elongation, respectively. The anchor is composed of a linear DEA and a force transmission mechanism. An applied voltage caused the DEA to elongate, decreasing the diameter of the anchoring unit. Thereby, if positioned in a pipeline, then the unit could reduce the normal force against the pipeline wall. When the voltage was turned off, the anchoring unit was restored to its prepressed normal force. To increase the friction between the anchoring feet and the pipeline wall, silicone adhesive (Sil-Poxy from Smooth-On Inc.) was used to form a shell on each anchoring foot with a thickness that could adjust the initial prepressure (with no voltage applied) of the anchoring unit in the pipeline. The Young's modulus (420 kPa at 100% strain) of DEA in the anchoring unit was relatively high, to provide sufficient anchoring force, whereas the Young's modulus (100 kPa at 100% strain) of DEA in the elongation unit was relatively low, so as to have an adequately soft body and large elongation. Three-dimensional (3D)–printed connectors equipped with magnets were used for the rapid assembly of different functional units (for anchor unit or elongation unit, see Fig. 1, B and C, and movie S1 for the rapid assembly process of the robot). The activation of the robot was by tethered cables powering each DEA separately.

For the use of the robot in real applications, we set the design objectives as follows: It could achieve both fast horizontal locomotion and vertical locomotion; move in pipes with curvatures; tolerate 1-mm variation of pipe diameter (specifically, 9 to 10 mm); and effectively move in pipes with coefficients of friction ranging from 0.1 to 0.5. To satisfy

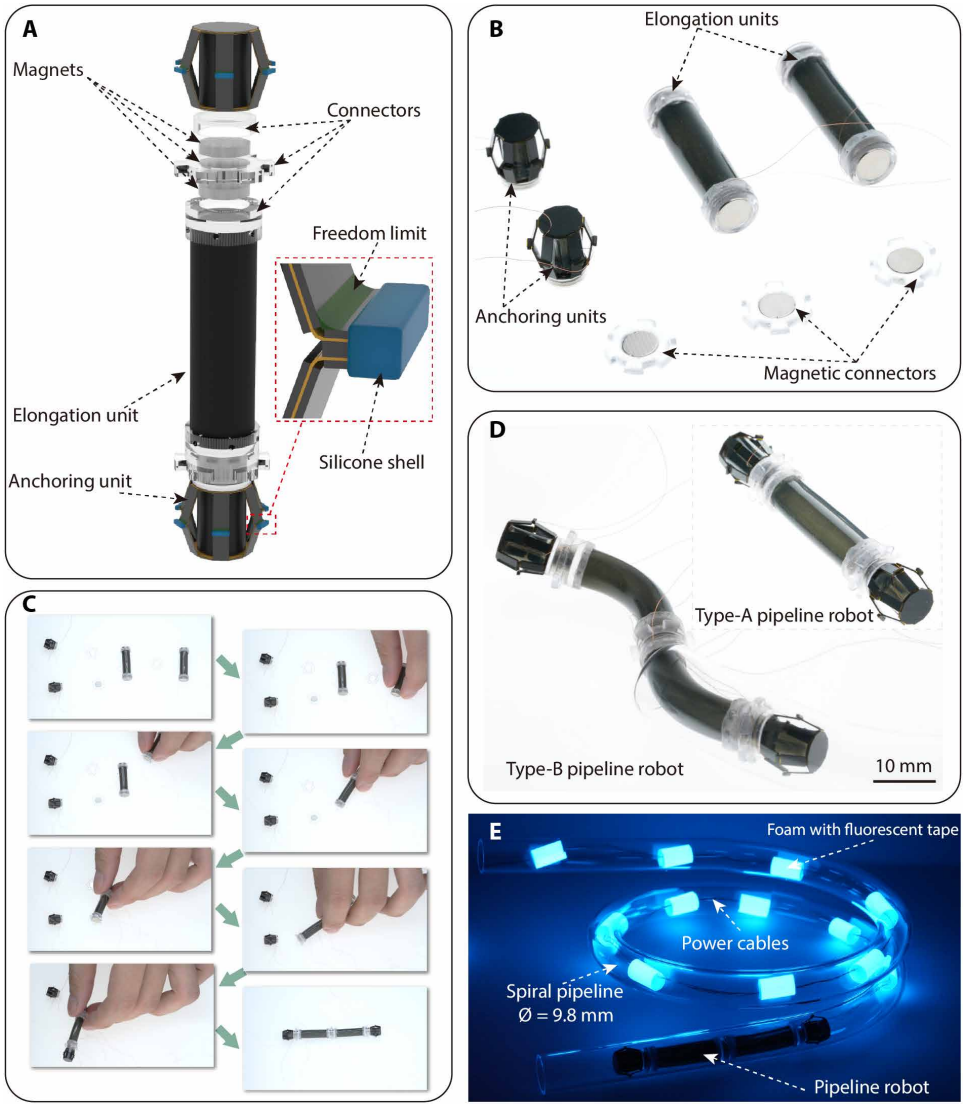

Fig. 1. Design and assembly of the proposed pipeline robot. (**A**) Schematic of the pipeline robot's structure (inset: a magnified schematic of a foot in the anchoring unit covered with silicone shell). (**B**) Compositional units of the pipeline robot: anchoring units, elongation units, and magnetic connectors. (**C**) The fast assembly process of a pipeline robot from different units. (**D**) Photos of two types of pipeline robots: two anchoring units and one elongation unit (Type-A), two anchoring units, and two elongation units (Type-B). (**E**) A tethered Type-B robot moving in a spiral pipeline in a dark environment.

the above objectives, we chose to use silicone-based dielectric elastomers (DEs) as the actuating components so as to rapidly control the anchors' motion and body's motion and used the materials' low Young's modulus to self-adapt to curved pipes. In addition, we designed the dimensions of the anchoring unit and the body actuator in Supplementary Methods, taking into consideration the kinematics and kinetics of the robot.

Using the determined parameters, two types of robot structures were then fabricated, assembled, and tested in this work. As shown in Fig. 1D, robot Type-A (weight, 2.2 g; length, 47 mm) contains two anchoring units and one elongation unit, and robot Type-B (weight, 3.4 g; length, 73 mm) is with two elongation units. For robot Type-A, high-speed horizontal and vertical pipeline movements were achieved, and for robot Type-B, successful navigation in L-shaped pipes, S-shaped pipes, and spiral-shaped pipes (Fig. 1E) was achieved, and all the pipes' diameters were within 10 mm. More elongation units can be added to form a longer body length of the pipeline robot.

Characterization and analysis of DEAs' performance

The fabrication process of the DEAs is shown in fig. S2 and described in the Supplementary Materials. The DEAs were first stacked to rectangular multilayers, consisting of 10 layers, each one being 50 μm thick, and then rolled into a cylindrical linear actuator (*23*). The two types of DE material properties are described in Materials and Methods. The DEA used for the elongation unit was 20 mm in length and 6 mm in diameter, whereas the DEA used for the anchoring unit was 7 mm in length and 5 mm in diameter. In the following parts, we characterized the static properties of the DEAs to check whether they met the design requirements in table S2 and then the dynamic properties for assisting the later control strategy design.

We investigated the static and dynamic performance of the DEA in the body elongation unit (Fig. 2, A to D). The testing setup is shown in fig. S3A and described in Materials and Methods. The driving voltage of this DEA ranged from 100 to 1200 V (which corresponded to an electric field slightly lower than the dielectric strength of the dielectric material), with an interval of 100 V in each step. As illustrated in Fig. 2 (A and B), the maximum displacement of the actuator was 1.5 mm (7.5% of strain) and the maximum block force of the actuator was 132 mN (0.5 N/cm^2), which met our requirement for body actuators in table S2. Figure 2C shows the actuator's frequency sweep of displacement in the range of 1 to 300 Hz, in 100 s at 1000 V. The actuator resonated at 105 Hz and had a harmonic resonance at 52 Hz. The displacement's time response of the elongation unit DEA at 1-, 50-, or 100-Hz sinusoidal wave with an amplitude of 1000 V and a bias of 500 V can be found in Fig. 2D. At low frequency, the displacement of the actuator was in phase with the driving voltage, yet as the driving frequency increased, the response of the actuator gradually lagged and ended up with a phase shift of 130° at 100 Hz due to the viscoelastic characteristic and inertia of the DE material. Considering its viscoelasticity and inertia, the actuator can be modeled as a mass-spring-damper system using the Kelvin-Voigt model (*23*) during actuating and follows

$$\sigma_a(l, U) = Y\varepsilon_a(l, U) + \eta\dot{\varepsilon}_a(l, U) + \frac{1}{2}\rho L^2\ddot{\varepsilon}_a(l, U) \quad (1)$$

where $\sigma_a(l, U)$ and $\varepsilon_a(l, U)$ are the stress and the strain of the actuator at height l and driving voltage U. Y is the Young's modulus of the DE material, L is the actuator's total length, η is the viscosity of the material, and ρ is its density.

Assume $\varepsilon_a(l, U)$ is homogeneous along the actuator's height, ignore the gravity of the actuator, and integrate both sides of Eq. (1) over l, we got

$$\frac{L}{S}F_a(U) = Y\Delta x + \eta\Delta\dot{x} + \frac{1}{2}\rho L^2\Delta\ddot{x} \quad (2)$$

where $\Delta x = \int_0^L \varepsilon_a(l, U)\,dl$ is the displacement of the actuator's end when the other end is fixed onto the ground, L and S are the length and cross-sectional area of the actuators, and F_a is the axial force caused from Maxwell stress and $F_a(U) = C_aU^2$. Experimentally, the force was consistent with the result in Fig. 2B, thus $C_a = 9.17 \times 10^{-8}$ N/V^2. To verify the model, we substituted the geometric parameters (L and S) and material properties (Y, η, and ρ) of the actuator (see the Supplementary Materials for the specific values of these properties) into the equations, numerically solved the time response of Δx with a sinusoidal voltage input ($U = U_a \sin(2\pi ft)/2 + U_a/2$) at different frequencies from 1 to 300 Hz (see the Supplementary Materials for the details of simulation using MATLAB), and simulated its frequency sweep as shown in Fig. 2C. The simulated frequency sweep was in great consistency with the experimental results, thus verifying the model to describe the DE material's properties. Later, the same material model was used to describe the pipeline robot's dynamic motions.

Similarly, we also characterized the mechanical performance of DEAs in the anchoring units, with the driving voltage ranging from 500 to 2000 V (Fig. 2, E to H). The displacement of the actuator was 130 μm (1.9% of strain), which was much smaller than that of the elongation unit; the maximum block force of the actuator was 255 mN (1.3 N/cm^2, which was almost three times larger than that of the elongation unit). In our assumptions, we ignored the damping and inertia of this type of actuator as in the frequency we cared about (0 to 300 Hz), neither its damping nor inertia made a notable effect. Therefore, we expected to see the amplitude of the actuator's displacement with frequency remained constant. Figure 2G presents the experimental sweep frequency of the actuator's free displacement at 1600 V amplitude from 1 to 300 Hz. The graph shows that the amplitude of displacement almost remained constant as our predictions. Unlike the displacement's time response at high frequency for the body elongation actuator in Fig. 2D, the phase delay in the anchoring unit's actuator was negligible (<10°) between 50 and 100 Hz, as shown in Fig. 2H, due to the relatively high modulus and small viscosity of its DE material. Therefore, in the pipeline robot's motion analysis, we ignored the dynamic lag in the anchor's motion with respect to its driving voltage even at high frequency and assumed that they were synchronized.

Design and performance test of the anchoring unit

The anchoring units need to transform the axial elongation/contraction of the DEA into the radial expansion/shrinking of the anchor's contact points (we name these contact points as feet) with the pipeline's inner wall. Here, we adopted a classical flextensional motion amplification structure (*30*) and designed six chains distributed equally along its circumference as shown in Fig. 1A. This 3D flextensional motion amplification structure was fabricated using SCM technology (*28*). Five layers of material with designed shapes were hot-pressed into a single piece of the composite structure (Fig. 3A) and then cut

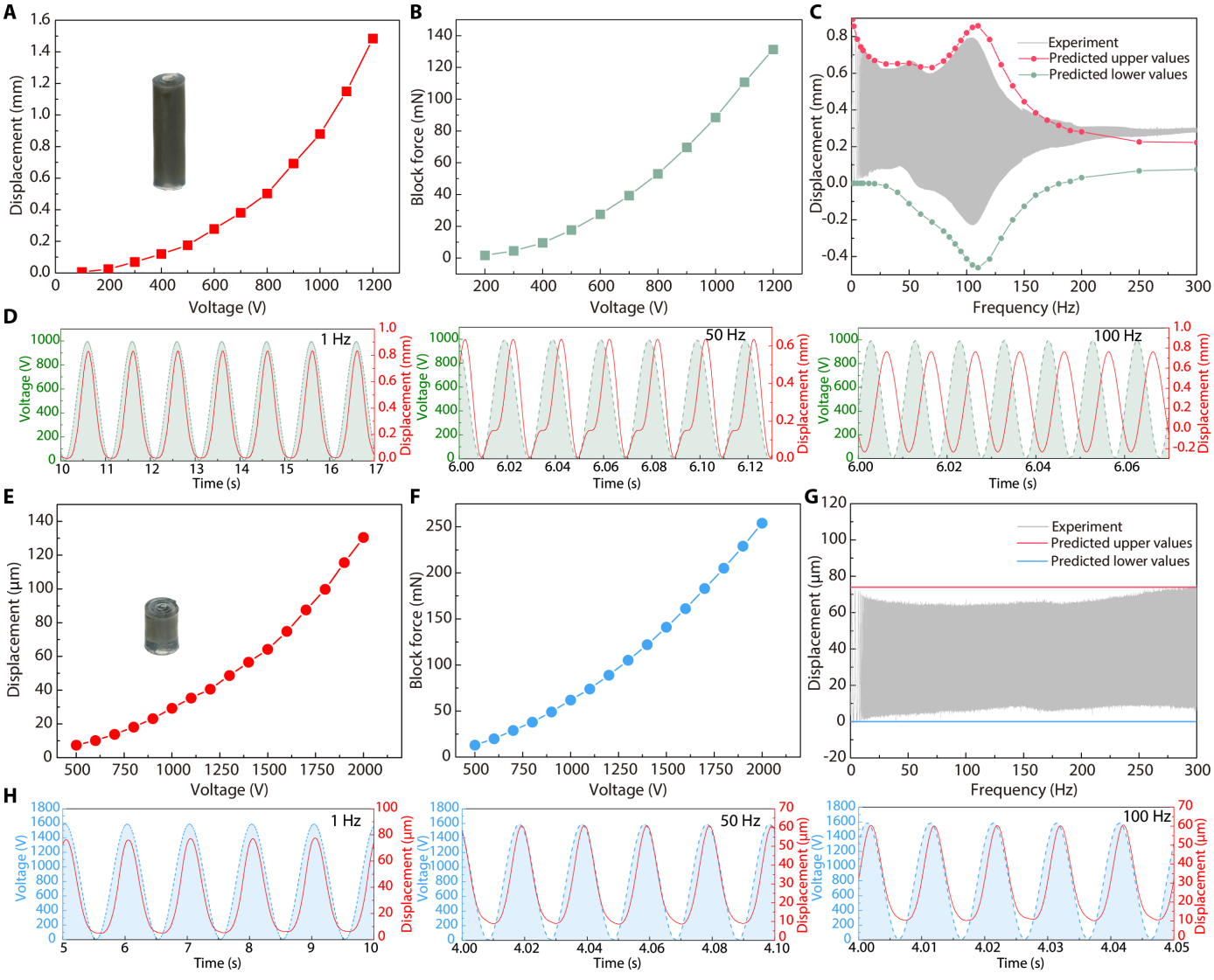

Fig. 2. Characterization of DEAs' mechanical performance. (**A**) Static output displacement of DEA used for elongation unit with voltages. (**B**) Static block force of DEA used for elongation unit with voltages. (**C**) Prediction and experimental results of the sweep frequency for the output displacement of DEA used for elongation unit. (**D**) Displacement's time response of the elongation unit's DEA driven by 1-, 50-, and 100-Hz sinusoidal voltages. (**E**) Static output displacement of DEA used for anchoring unit with voltages. (**F**) Static block force of DEA used for anchoring unit with voltages. (**G**) Prediction and experimental results of the dynamic sweep-frequency output displacement of DEA used for anchoring unit. (**H**) Displacement's time response of anchoring unit's DEA driven by 1-, 50-, and 100-Hz sinusoidal voltages.

along the cutting path to release the flexible hinge structure (details of the SCM process are described in Materials and Methods and fig. S6). Two pieces of these flexible hinge structures and one DEA were assembled into one anchor unit. Considering that the carbon fiber layer of the flexible hinge structure was conductive, the DEA was first adhered to polyimide film with highly conductive silver epoxy adhesive and then adhered to the flexible hinge with 3M VHB9460 to avoid short circuit. The two pieces of flexible hinges, after positioning, were bonded together using instant adhesives, and then the excessive positioning structure was cut off. The degrees of freedom for the fabricated 3D flextensional motion amplification structure was seven, and thus instant adhesive was applied to the forward side of each foot to limit the final mechanism's degree of freedom to one (see the inset image in Fig. 1A).

The finalized design of the anchoring unit is shown in Fig. 3B, and the weight of the anchoring unit was 220 mg. The linear motion of the actuator transformed to the radial motion of the structure's feet (see movie S2), and if blocked, the linear block force of the DEA transformed to the feet's normal force with the pipeline walls.

Assuming all parts of the structure were rigid components except the flexible joints (Fig. 3B), the theoretical kinetic relationship between the anchor's output force f in the radial direction of a single anchor foot and the DEA's generated axial force F was as follows: $f = F/3 \tan \theta$, where $\theta = 71°$ with our geometric design. The force on one anchoring foot, as calculated by the theoretical formula, was 11.5% of the DEA's output force. A COMSOL model was established to perform static mechanics analysis of the manufactured anchoring component to verify if we took into consideration the deformation

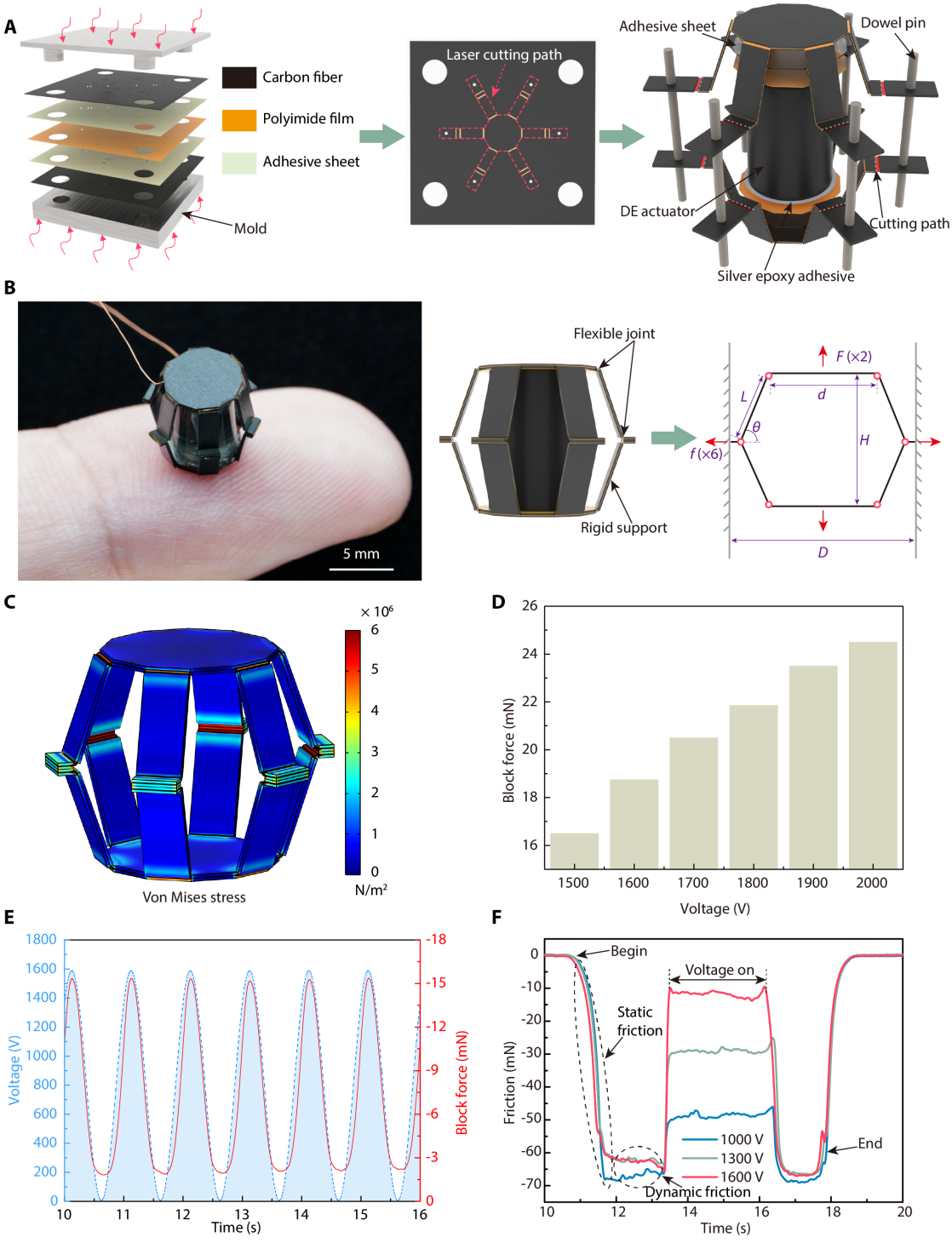

Fig. 3. Fabrication process and performance test of anchoring unit. (**A**) Anchoring unit manufacturing process. (**B**) Photograph of the anchoring unit on a human fingertip and its free body diagram. *F* is the actuator's axial force (two of them) and *f* is the feet force from the pipe wall (six of them). (**C**) Finite element analysis model of mechanical force transmission. (**D**) Block force of a single anchor foot at different voltages. (**E**) Dynamic force output of a single anchor foot at 1 Hz. (**F**) Dynamic frictional force test under different applied voltages of an anchor.

of all the components, whether the force could be transformed efficiently. In COMSOL, we established a model with the exact material and geometry we used in our experiment. The bottom of the anchoring component was fixed, the six feet were constrained to only axial displacements (no radial displacements), and a constant force was applied on the top of the anchoring component vertically upward (to simulate the force generated from DEA). Figure 3C shows the von Mises stress distribution of the whole structure in response to

the applied force, and we simulated the reactive force onto each foot in the radial direction. With our chosen materials and geometric designs, the force transferred efficiently, with a simulated ratio of 12.2%, which was in good consistency with the theoretical predictions. This consistency indicates that our material choice and geometric parameters (especially the length and thickness of the rigid segments) can ensure an expected transmission of force from the DEA to the feet.

We then experimentally characterized the anchoring unit's capability for adjusting friction. We measured the output force of a single anchoring foot under different applied voltages of DEA (Fig. 3D). The experimental setup for this measurement is shown in fig. S3B. A comparison of the illustrated results in Figs. 2F and 3D shows that the actual force transfer efficiency from DEA to a single foot was 10.9%, which was consistent with the theoretical value, further demonstrating the effectiveness of the anchoring unit. We also measured the dynamic force output of a single anchor foot with a 1-Hz sinusoidal voltage (Fig. 3E). In the proposed robot design, control of the friction between the anchors and the pipeline wall was the most critical point for efficient locomotion. Therefore, an experimental platform was established to test the friction-controlling capability of the anchoring unit in the pipeline (fig. S3C and Materials and Methods). In this platform, a linear motor drove the sliding table to move at a constant speed of 10 mm/s, and a force sensor was installed on the sliding table and connected to the anchoring unit in the pipeline through a nylon thread. One measured friction curve of our designed anchoring unit with silicone shells in a glass pipe of 9.8 mm at different driving voltages is shown in Fig. 3F. Once the motor started to operate, the nylon thread was in tension, and the friction measured by the sensor rose rapidly. Next, the voltage was applied and the normal force between the anchoring unit and the pipeline wall, thus the measured dynamic friction, decreased immediately. Last, when the voltage was turned off, the friction returned to the initial value. The friction adjustment range rose to 51 mN at 1600 V. In movie S2, we also intuitively showed the anchor's capability to withstand weight and the capability to adjust this maximum weight via voltage. The friction of the anchoring unit with other types of pipes used in the paper was also measured in fig. S4, and the coefficients of friction were calculated as 0.45 ± 0.01, 0.32 ± 0.02, and 0.18 ± 0.03 with glass, metal, and carbon fiber, respectively. We tested the robot's locomotion in different types of pipes in later sections.

Motion analysis and control of Type-A pipeline robot

We took the Type-A pipeline robot as an example and established a dynamic model to analyze its motion in straight pipelines. Figure 4A describes the form and phase of the driving voltages applied to all units of the Type-A robot. The front and rear anchoring units were

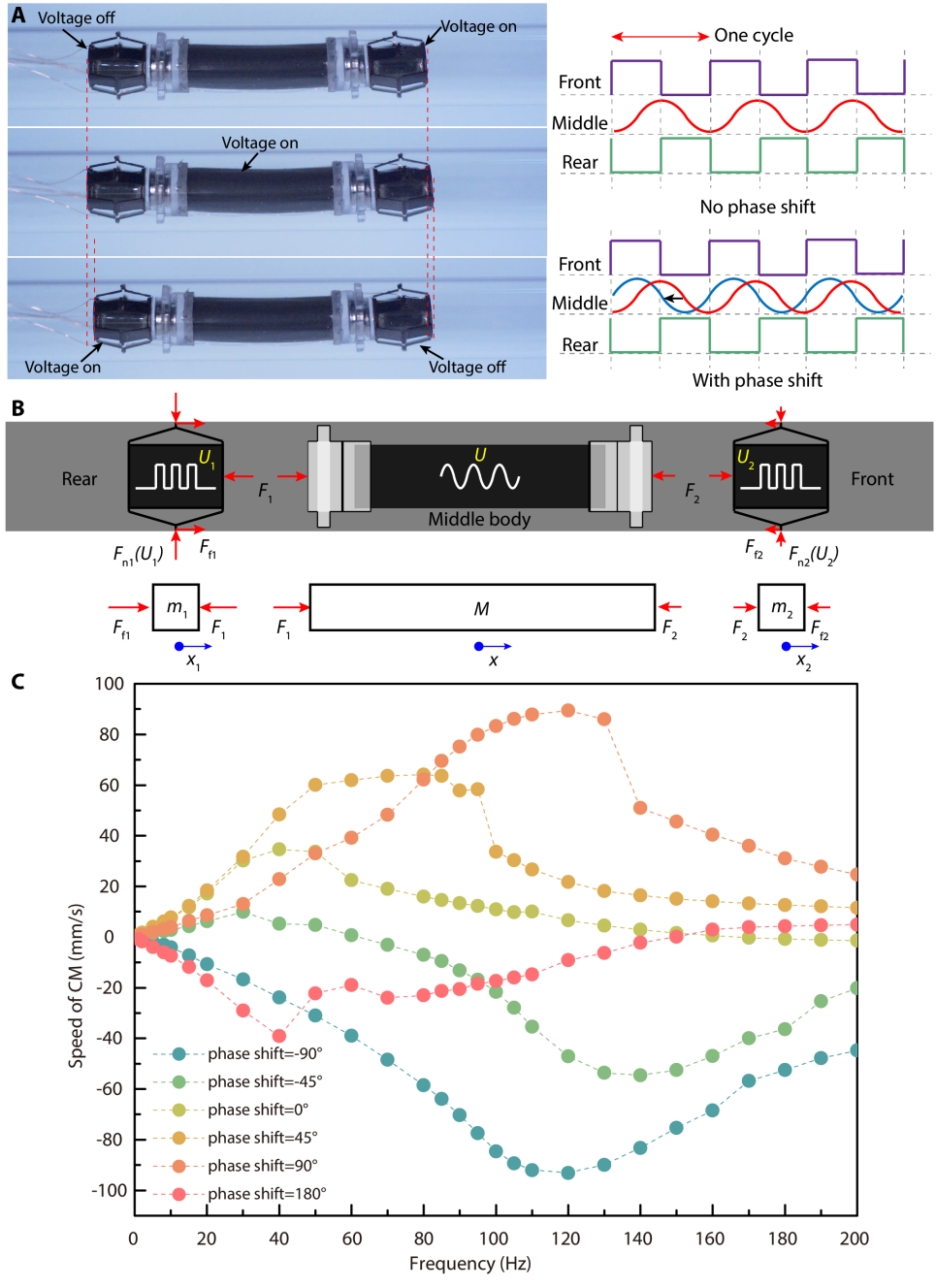

Fig. 4. Motion analysis of Type-A pipeline robot. (**A**) Basic motion of the robot within a cycle and the driving signals. (**B**) Free-body diagrams of separate parts of the robot. (**C**) Frequency and phase map of the simulated speed of CM for the robot.

driven by square-wave voltages, and the middle elongation unit was driven by a biased sinusoidal-wave voltage. The baseline phases of the front anchoring, elongation, and rear anchoring units were 0°, 270°, and 180°, respectively. During the elongation of the middle body, the front anchoring unit was released and the rear anchoring unit was anchored, and during the shrinking of the middle body, the front anchoring unit was anchored and the rear anchoring unit was released, causing the center of mass (CM) of the body to move forward in both procedures. When the middle elongation unit was driven by a sinusoidal voltage signal, the front and rear anchoring units' motion was as expected: anchoring at a low-level signal and slipping at a high-level signal. However, if the middle elongation unit was driven by a square wave–shaped voltage signal, then both the front and the rear anchoring units slipped whatever the applied voltage was, causing ineffective movement of the robot during the whole process (see movie S3). The main reason was that the instantaneous loading of the elongation DEA's driving force would be exerted onto both anchors immediately, and this contact force was larger than the maximum static friction of the anchored unit, thus causing slippage even for the anchored unit. Gradually increasing the elongation DEA's driving force (for example, using sinusoidal wave) would ensure that the contact force between the anchor and the body was reduced due to the DEA's elongation; thus, it was essential to achieve the expected motions of the robot.

The above process was only applicable for quasi-static cases of activation when the applied voltage was of low frequency. Ideally, the moving speed of the robot should scale up with driving frequency. However, at high-frequency activation, the soft materials' viscoelasticity and inertia caused a marked phase shift between its applied voltage and the output deformation and had a nonnegligible influence on the robot's motion. Thus, we had to carefully tune the phase shift of the driving voltages for all units as shown in Fig. 4A. We modeled how these unique characteristics affect the robot's motion in straight pipelines.

The detailed assumptions and derivation of the model can be found in Supplementary Methods. We first formed the free body force balance equations of the body, front anchoring unit, and rear anchoring unit (free body diagrams are shown in Fig. 4B), and then we established the equation of the body's deformation caused by Maxwell stress, inertial stress, and external forces. Next, we substituted the boundary conditions for the robot based on its actual status. We used MATLAB to numerically solve the robot's motion over time, at various frequencies (from 1 up to 200 Hz) and phases (−90°, −45°, 0°, 45°, 90°, and 180°, for U, with respect to the baseline driving signals described in Fig. 4A) of the driving signal (U_1, U_2, and U). All parameters used for this computation were based on experimental characterization of the actuating materials, anchoring structures, and real parameters measured for the robots (see table S3).

The simulated displacement and velocity of the robot's body, front anchor, and rear anchor at 1, 10, and 100 Hz with no phase correction (0°, 270°, and 180° phase for U_1, U, and U_2) are shown in fig. S8. It could be seen that at 1 and 10 Hz, the robot performed almost identical motions and moving distance for each cycle. Yet, at 100 Hz, the robot's rear anchor had severe slippage caused by phase deviation of its body elongation from the original planned pace (body elongated when the rear anchor was fixed and the front anchor was released and contracted when the rear anchor was released and the front anchor was fixed). Changing the phase of the body elongation DEA could markedly affect the robot's motion. At a phase shift of −45°, the robot could even move backward, and at a phase correction of 90°, the robot could move forward five times faster than without phase correction. Figure 4C gives a full map of the robot's CM speed at different frequencies and phases. It indicates that to maximize the robot's moving speed, not only the frequency but also the phase correction plays critical roles. However, although very enlightening, this motion simulation is based on very strict assumptions that might change in practical experiments. Thus, the optimal combinations of frequency and phase to optimize the robot's speed should be experimentally tuned.

Motion test of the pipeline robots in various environments

We first tested the Type-A robot's motion in straight pipes with a diameter of 9.8 mm. Three voltage signals (U_1, U_2, and U; Fig. 4B) were generated by LabVIEW and then sent to a Trek 2220 high-voltage amplifier, through NI USB-6363 (fig. S9), to be applied to the robot through the enameled wire (Elektrisola-G3; 0.053 mm in diameter). For the frequency sweep, three signals (U_1, U_2, and U) applied to the rear anchor, front anchor, and body DEAs had amplitudes of 1600, 1600, and 1200 V and phases of 0°, 180°, and 270°, respectively, at frequencies ranging from 1 to 150 Hz. According to the result of the speed test (Fig. 5A), when there was no phase correction, the speed of the robot first increased with the increase in the driving frequency and then slowed down until it started to move quickly in the opposite direction, followed by gradually slowing down again, after reaching a peak speed. As expected from the motion analysis, the fact that the responses of the three DEAs were not synchronized at high frequency was an important factor affecting the speed of the robot, as shown in Fig. 5B. The trajectories of the robot's front and rear anchoring unit are also shown in Fig. 5B, as recorded by a high-speed camera (Phantom VEO-E 310L from Vision Research Inc.). At the driving frequencies of 1, 10, and 20 Hz, the motion trajectories of the robots were as expected in low-frequency cases, with the front and rear anchoring units alternatively moving forward with negligible backward motions. At the driving frequency of 60 Hz, the backward sliding of the rear anchoring unit of the robot was much more obvious, and the robot's moving displacement in each cycle was markedly smaller than that at low frequencies. At 100 Hz, the robot started to move backward. The motion direction of the robot could be shifted by changing the phase of the elongation unit by 180° (movie S4). After correcting the phase, the robot could achieve a fast forward speed (maximum 1.19 body lengths/s at 110 Hz), whereas before correcting the phase, a fast backward speed could be reached (maximum 1.17 body lengths/s at 120 Hz), as shown in Fig. 5A. We have experimentally demonstrated how varying the frequency and phase could markedly affect the speed of the robot moving in pipelines. We also tested and measured the speed of the robot climbing a pipe vertically oriented, and this was found to be 51 mm/s (1.08 body lengths/s) at 100 Hz (movie S7).

Here, we draw a map showing the applicable pipeline's diameter and pipeline robot's locomotion speed in the pipe with different actuating methods including electromagnetic motors (*31*–*36*), piezoelectrics (*37*–*39*), SMAs (*40*–*43*), and fluidic elastomer actuators (*44*–*55*) (Fig. 5C). We separately compared the horizontal speed and vertical speed of different types of pipeline robots (Fig. 5C). The pipeline robot driven by DEAs proposed in this paper realized rapid movement (which is piezoelectric-material-driven

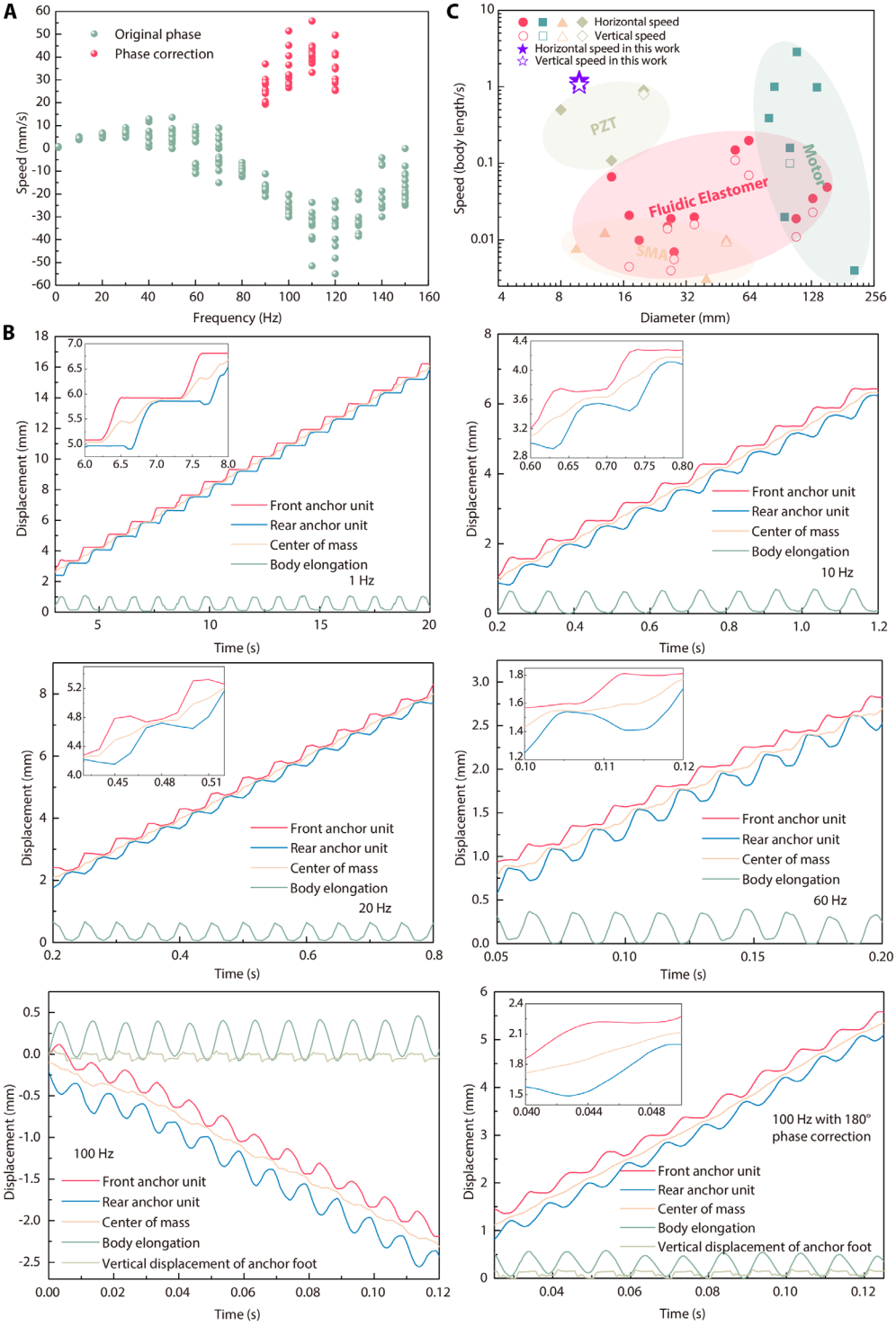

Fig. 5. Motion test results of the pipeline robot. (**A**) Motion speed of robot under different driving frequencies and phases. (**B**) The trajectories and speeds of the robot's front and rear anchoring units at 1, 10, 20, 60, 100, and 100 Hz with 180° phase correction. (**C**) Comparison of pipeline dimension and moving speed (horizontal solid symbols and vertical hollow symbols) of pipeline robots with different actuating mechanisms and materials.

robots comparable) in the sub-centimeter pipeline, and its highly soft body could adapt to more complex pipeline shapes by simply reconfiguring the robot segments.

We tested the movements of the Type-A robot in the horizontal direction (Fig. 6A and movie S5) and in the 90° vertical direction at 1- and 100-Hz driving voltages (Fig. 6B and movie S6). We examined the robot's adaptability in several pipe conditions (for example, varying internal diameter, pipe material, and the presence of a medium). We tested the robot navigated along a horizontal pipe filled with insulating oils at 1, 5, 10, 20, and 90 Hz (Fig. 6C and movie S7). Although the friction was markedly reduced due to the oil, the robot still achieved effective locomotion after we carefully tuned its frequency and phase. The robot could also navigate in a diameter-varying pipe (Fig. 6D and movie S8). The pipe had a smoothly changing diameter from 10 to 9 mm and back to 10 mm. The robot successfully navigated through the pipe at a fixed frequency of 100 Hz and a phase correction of 90°. It was clear from the movie that the velocity of the robot decreased in the 9-mm segment, due to the increased normal force and friction from the anchoring units. We tested the robot's motion at a carbon fiber pipe at 1, 10, and 100 Hz and recorded its motion from a camera installed at the end of the pipe, as shown in Fig. 6E and movie S9. The above three demonstrations showed the robot's capability to adapt to different pipe surface conditions and geometries. One key point is that the velocity of the robot was severely affected by the change of geometry and pipe material's coefficient of friction, and thus finer tuning of its driving frequency and phase is essential to achieving efficient locomotion. Now, we achieved such tuning manually. If the robot could adaptively adjust the driving voltage and phase according to the pipeline environment, then its motion capability would be further improved. Last, to demonstrate the robot's practical application in pipeline inspection, we equipped the robot with an endoscope camera (EZ-EN45S from Yichuang Electronics; 200 mg) at its front anchoring unit and performed a remotely controlled inspection in a closed metal pipe with a diameter of 9.8 mm (Fig. 6F and movie S10). With a 1-Hz driving signal, the robot moved along

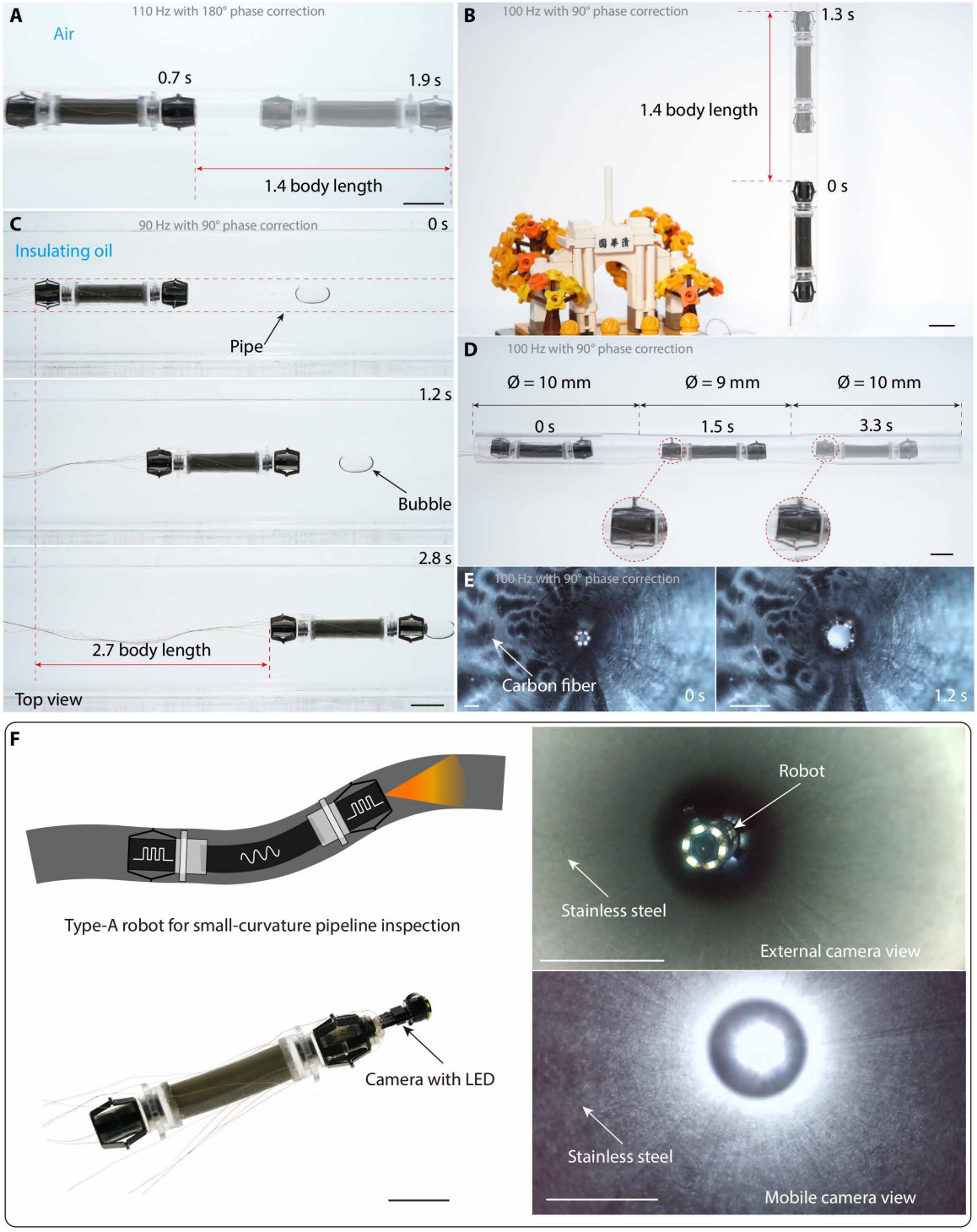

Fig. 6. Demonstrated motions of Type-A robot in pipes. (**A**) Photographs of the robot moving at a high speed in a horizontal pipeline. (**B**) Photographs of the robot moving in a 90° vertical pipeline with a driving frequency of 100 Hz. (**C**) Photographs of the robot navigating in a pipe filled with liquid oil. (**D**) Photographs of the robot navigating in a pipe with changing internal diameters (10 to 9 to 10 mm). (**E**) Photographs of the robot navigating in a pipe made of carbon fiber. (**F**) Images of the robot with a camera installed at the front and the robot inspecting the environment in a stainless steel pipe at a driving frequency of 1 Hz. Scale bars, 10 mm.

the pipe slowly, and from the onboard camera view, the detailed topology and texture of the pipe's inner wall could be clearly monitored and recorded. At higher frequencies of 30 and 100 Hz, the robot moved rapidly in the metal pipeline, but the images from both two cameras were shaking violently and blurred due to the robot's markedly moving speed. An anti-shake device and a high-speed camera are necessary to obtain clearer images for high-speed pipeline inspection.

The robot with one elongation unit (Type-A) achieved fast motion in straight pipelines, but in pipelines with curvature, the anchoring units could hardly be concentric with the pipe axis, thus reducing the anchoring normal forces. Our robot was designed with soft, elastic materials, and thus, with enough force applied, it could be bent to different shapes. When the robot was in a curved pipe, it passively adapted to the shape of the pipe by deforming, and the deformation was due to the reaction forces from the pipe walls to the anchors at two ends. We modeled our robot as a bending beam with modulus E, bending moment inertia I, and length L; then, if a load P was applied on one of its ends and the other end was fixed, we could get the bending curvature $\kappa = \frac{PL}{EI}$. Therefore, the bending flexibility was as $\frac{\kappa}{P} = \frac{L}{EI}$. From this equation, it could be seen that large L led to larger flexibility. With more elongation units assembled, the flexibility of the robot could be increased, thus improving the concentricity of the anchoring units and subsequently the anchoring forces. We tested the Type-B robot's mobility in straight and curved pipes (Fig. 7). The robot could achieve rapid, horizontal motions as the Type-A robot, and by tuning its phase, it could realize bidirectional motions (movie S11). Type-B robot with two segments of the elongation units successfully navigated through an S-shaped pipe

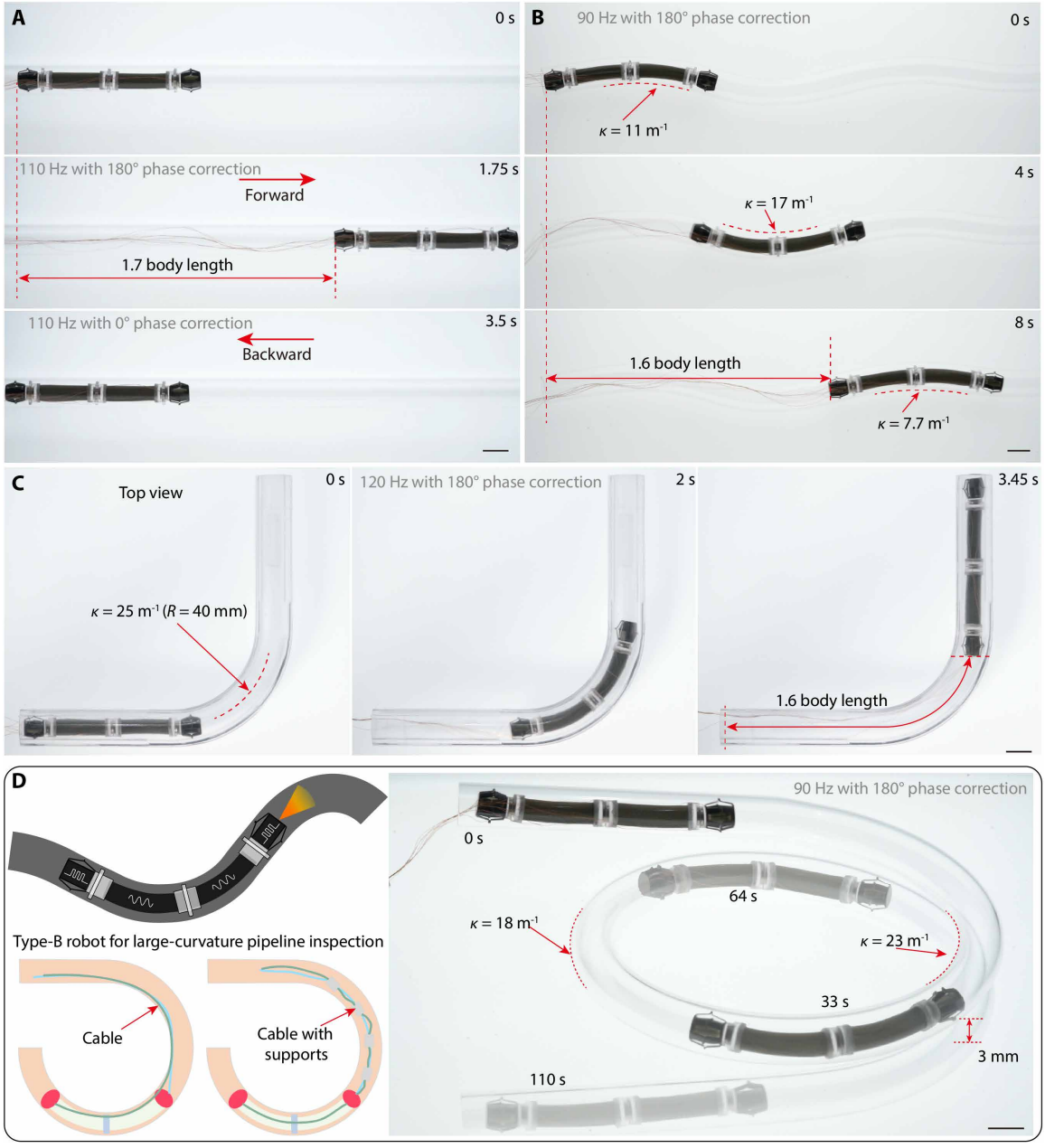

Fig. 7. Demonstrated motions of Type-B robot in curved pipes. (**A**) Bidirectional horizontal motions of the robot. (**B**) The robot navigated in an S-shaped pipe with varying curvatures. (**C**) The robot navigated in an L-shaped pipe with a bending radius of 40 mm (curvature, ~25 m^{-1}). (**D**) Schematic diagram and photographs showing the robot went through a spiral pipe for inspection. Bottom left image: Schematic diagram of robot's tethers without and with supports. Scale bars, 10 mm.

with an average speed of 14.5 mm/s (Fig. 7B and movie S12). The curvature of the pipe ranged from 7.7 to 17 m^{-1}, and its diameter was about 10 mm as well. Note that the speed of the robot was much slower than that in straight pipes, and this was because the deviation in inner diameters of the S-shaped pipe made from hand bending was up to 0.5 mm. The reduction of diameter caused an increase in friction and thus a decrease in speed. To investigate the maximum curvature with which the Type-B robot could navigate, we 3D printed a series of L-shaped pipes with different turning radii and uniform internal diameters. The robot successfully navigated an L-shaped pipe with a turning radius of 40 mm (curvature, ~25 m^{-1}), at a speed of 0.46 body length/s (Fig. 7C and movie S13).

In the case of straight pipe, the electric cables for powering and controlling the pipeline robot generated a drag force of about 1.6 ± 0.2 mN/m (see fig. S5), which could be overcome by the actuator's force at a distance of less than 10 m. Yet, in the case of a spiral pipe, the force from the cables severely slowed down its speed due to the accumulated friction along a long path. The cables became tighter as the robot moved deeper into the pipeline; in addition, the drag force from the cables also affected the concentricity of the anchoring units with the pipe and eventually completely restricted the robot's forward motion (Fig. 7D). To solve this problem, we used small cylinders made of polyethylene foam to wrap the cables at intervals (Fig. 7D), reducing the friction and facilitating the tethered robot to move into deep pipes. Last, the robot successfully navigated a spiral pipe with a diameter of 100 mm and a pitch of 3 mm (Fig. 7E and movie S14), which took about 110 s. Although it navigated the pipe at a relatively low speed, the robot's capability to overcome curved pipes with a curvature of up to 23 m^{-1} and a distance of more than 60 cm showed the potential for deployment in other complex pipelines.

DISCUSSION

In this work, we have demonstrated the feasibility of rapidly assembling and constructing a tethered, subcentimeter-diameter–scale pipeline inspection robot using smart materials and structures. Specifically, soft dielectric elastomer materials were used for actuating, and compliant composite structures were used for transmitting force. We demonstrated its high-speed characteristics in horizontal and vertical straight pipelines through frequency and phase modulation and overcoming some specific challenges due to soft material properties (for example, viscoelasticity). We have also demonstrated the robot's unique capability of passively adapting to curved pipelines with a second configuration of the robot through its compliant body. In addition, the robot also exhibited a certain level of adaptability to changing pipe diameters, materials, and filled media. Compared with other types of pipeline robots (*31*–*55*), the robot designed in this paper showed higher environmental adaptability and achieved high-speed navigation, especially on the sub-centimeter scale. For its practical application, we have shown a preliminary demonstration of our tethered robot to navigate a metal pipe and record images, showing the potential applications for pipeline inspection in complex systems. Although very promising, there remain several aspects to further optimize the design and driving method of our pipeline robot. Now, the robot can only adapt to a limited range of diameters (within 1 mm) due to the anchoring design and the actuator's force output. Anchoring units with a larger range of diameter adaptability and higher–energy density actuators are necessary to further improve the robot's locomotion. The turning radius of the robot is now large, and in the future, we hope to explore actuators with active bending capability by patterning the electrodes (*56*) or adding more segments to form a more flexible robot. In addition, the robot's high-voltage power is now provided via cables, which might cause the problem of large drag force that prevents the robot from going deeper into pipes. Small high-voltage power supplies and high–energy density batteries (*57*) might be used to render the robot untethered and autonomous.

MATERIALS AND METHODS

Materials for the fabrication of the DEA and electrodes

The dielectric elastomer used for the actuator in the elongation unit was composed of Smooth-on Ecoflex 0030 (1:1) and Dow Corning Sylgard 184 (40:1), at a mixture ratio of 1:1. The dielectric elastomer of DEA used for the anchoring unit was composed of Elkem Silbione LSR 4305 (1:1) and Sylgard 184 (10:1), at a mixture ratio of 3:1. The electrode material used in this work was ultrapure single-walled CNT aqueous dispersion (0.15 weight %) by Nanjing XFNANO Materials Tech. The original solution was diluted 100 times, and 0.75 ml (equivalent areal density is 2.5×10^{-9} g mm^{-2}) was used for each layer of the electrode.

Mechanical performance characterization of DEAs and anchoring units

The experimental setup for characterizing the output force and displacement of two types of DEAs is in fig. S3A. A laser displacement sensor (LK-H050 from Keyence Corporation) and a force sensor (Angewandte System Technik, LA-LF2.5N) were used in this study. Figure S3B illustrates a schematic diagram of the experimental setup for measuring the voltage-induced output force of one foot when blocking all other five feet of the anchoring unit. Figure S3C illustrates a schematic diagram of the experimental setup for measuring the anchoring unit's voltage-induced dynamic friction in a 9.8-mm glass pipe using a force sensor (GSO-100 from Transducer Techniques). A linear motor was used to drag the anchoring unit through a nylon thread at a constant speed. The thread was initially loose and then in tension, then the voltage was applied to the anchoring unit for a while, and, later, power was off. Last, the motor stopped moving. The tensional force of the thread was recorded during the whole process through the force sensor.

SCM fabrication

A 355-nm picosecond ultraviolet laser cutting machine (Wuhan Hero Optoelectronics Technology Co. Ltd.) was used to fabricate the designed shape on the different materials (the shape and dimension of the 2D microstructure are in fig. S6). The carbon fiber composite was laminated by curing three-layer carbon fiber prepregs (the orientations of the fibers in the three layers were 0°, 90°, and 0°, and the total thickness was 100 μm). A single-layer carbon fiber composite was anisotropic; therefore, one of the two-layer carbon fiber composites in Fig. 3A needed to be rotated by 90° during processing, to realize the isotropy of the composite structure, after hot press. The DuPont Pyralux FR0100 (25 μm) was used as sheet adhesive, and the polyimide film (DuPont Kapton 100HN; with a thickness of 25 μm) was used as the flexible connection material. After stacking the five layers in a stainless steel mold, the multilayer was placed in a heated press for bonding (190°C, 2 hours at a pressure higher than 400 kPa). The anchoring structure from the above steps was connected

to a DEA through a thin adhesive film of 3M VHB9460 (50 μm). The Young's modulus, Poisson's ratio, and density of the carbon fiber composite were 588 GPa, 0.3, and 1930 kg/m^3, respectively. The Young's modulus, Poisson's ratio, and density of the polyimide film were 2.6 GPa, 0.34, and 1420 kg/m^3, respectively.

Statistics

During the measurement of coefficients of friction between the anchoring unit and different pipes (fig. S4), 1500 samples of dynamic friction during voltage off and 1500 samples during voltage on were collected, and each set of 1500 samples was used to calculate the mean and SD of their difference. Then, coefficients of friction were calculated by the mean and SD of the difference in dynamic friction dividing the difference in normal forces during voltage on and off. During the measurement of drag force caused by the cables with the pipes (fig. S5), 1500 samples of the dynamic friction were also collected, and the mean and SD were calculated from these 1500 samples.

SUPPLEMENTARY MATERIALS

www.science.org/doi/10.1126/scirobotics.abm8597
Supplementary Methods
Figs. S1 to S9
Tables S1 to S3
Movies S1 to S14

REFERENCES AND NOTES

1. H. R. Choi, S. M. Ryew, Robotic system with active steering capability for internal inspection of urban gas pipelines. *Mechatronics* **12**, 713–736 (2002).
2. A. Zagler, F. Pfeiffer, " MORITZ" a pipe crawler for tube junctions, in *2003 IEEE International Conference on Robotics and Automation (Cat. No. 03CH37422)* (IEEE, 2003), vol. 3, pp. 2954–2959.
3. L. Xu, L. Zhang, J. Zhao, K. Kim, Cornering algorithm for a crawler in-pipe inspection robot. *Symmetry* **12**, 2016 (2020).
4. C.-Y. Yeh, C.-Y. Chen, J.-Y. Juang, Soft hopping and crawling robot for in-pipe traveling. *Extreme Mech. Lett.* **39**, 100854 (2020).
5. X. Ji, X. Liu, V. Cacucciolo, M. Imboden, Y. Civet, A. El Haitami, S. Cantin, Y. Perriard, H. Shea, An autonomous untethered fast soft robotic insect driven by low-voltage dielectric elastomer actuators. *Sci. Robot.* **4**, eaaz6451 (2019).
6. C. Tang, W. Ma, B. Li, M. Jin, H. Chen, Cephalopod-inspired swimming robot using dielectric elastomer synthetic jet actuator. *Adv. Eng. Mater.* **22**, 1901130 (2020).
7. R. F. Shepherd, F. Ilievski, W. Choi, S. A. Morin, A. A. Stokes, A. D. Mazzeo, X. Chen, M. Wang, G. M. Whitesides, Multigait soft robot. *Pro. Natl. Acad. Sci. U.S.A.* **108**, 20400–20403 (2011).
8. H. Zhao, K. O'Brien, S. Li, R. F. Shepherd, Optoelectronically innervated soft prosthetic hand via stretchable optical waveguides. *Sci. Robot.* **1**, eaai7529 (2016).
9. Y. Wang, X. Yang, Y. Chen, D. K. Wainwright, C. P. Kenaley, Z. Gong, Z. Liu, H. Liu, J. Guan, T. Wang, A biorobotic adhesive disc for underwater hitchhiking inspired by the remora suckerfish. *Sci. Robot.* **2**, eaan8072 (2017).
10. H. Yuk, S. Lin, C. Ma, M. Takaffoli, N. X. Fang, X. Zhao, Hydraulic hydrogel actuators and robots optically and sonically camouflaged in water. *Nat. Commun.* **8**, 14230 (2017).
11. H.-T. Lin, G. G. Leisk, B. Trimmer, GoQBot: A caterpillar-inspired soft-bodied rolling robot. *Bioinspir. Biomim.* **6**, 026007 (2011).
12. W. Wang, N.-G. Kim, H. Rodrigue, S.-H. Ahn, Modular assembly of soft deployable structures and robots. *Mater. Horiz.* **4**, 367–376 (2017).
13. S. Li, H. Bai, Z. Liu, X. Zhang, C. Huang, L. W. Wiesner, M. Silberstein, R. F. Shepherd, Digital light processing of liquid crystal elastomers for self-sensing artificial muscles. *Sci. Adv.* **7**, eabg3677 (2021).
14. Y. Kim, G. A. Parada, S. Liu, X. Zhao, Ferromagnetic soft continuum robots. *Sci. Robot.* **4**, eaax7329 (2019).
15. Y. Kim, H. Yuk, R. Zhao, S. A. Chester, X. Zhao, Printing ferromagnetic domains for untethered fast-transforming soft materials. *Nature* **558**, 274–279 (2018).
16. L. Hines, K. Petersen, G. Z. Lum, M. Sitti, Soft actuators for small-scale robotics. *Adv. Mater.* **29**, 1603483 (2017).
17. J. Zhang, J. Sheng, C. T. O'Neill, C. J. Walsh, R. J. Wood, J.-H. Ryu, J. P. Desai, M. C. Yip, Robotic artificial muscles: Current progress and future perspectives. *IEEE Trans. Robot.* **35**, 761–781 (2019).
18. F. Carpi, D. De Rossi, R. Kornbluh, R. E. Pelrine, P. Sommer-Larsen, *Dielectric Elastomers as Electromechanical Transducers: Fundamentals, Materials, Devices, Models and Applications of an Emerging Electroactive Polymer Technology* (Elsevier, 2011).
19. D. Rus, M. T. Tolley, Design, fabrication and control of soft robots. *Nature* **521**, 467–475 (2015).
20. Y. Chen, H. Zhao, J. Mao, P. Chirarattananon, E. F. Helbling, N.-S. P. Hyun, D. R. Clarke, R. J. Wood, Controlled flight of a microrobot powered by soft artificial muscles. *Nature* **575**, 324–329 (2019).
21. G. Gu, J. Zou, R. Zhao, X. Zhao, X. Zhu, Soft wall-climbing robots. *Sci. Robot.* **3**, eaat2874 (2018).
22. G. Li, X. Chen, F. Zhou, Y. Liang, Y. Xiao, X. Cao, Z. Zhang, M. Zhang, B. Wu, S. Yin, Y. Xu, H. Fan, Z. Chen, W. Song, W. Yang, B. Pan, J. Hou, W. Zou, S. He, X. Yang, G. Mao, Z. Jia, H. Zhou, T. Li, S. Qu, Z. Xu, Z. Huang, Y. Luo, T. Xie, J. Gu, S. Zhu, W. Yang, Self-powered soft robot in the Mariana Trench. *Nature* **591**, 66–71 (2021).
23. H. Zhao, A. M. Hussain, M. Duduta, D. M. Vogt, R. J. Wood, D. R. Clarke, Compact dielectric elastomer linear actuators. *Adv. Funct. Mater.* **28**, 1804328 (2018).
24. X. Dong, C. Tang, S. Jiang, Q. Shao, H. Zhao, Increasing the payload and terrain adaptivity of an untethered crawling robot via soft-rigid coupled linear actuators. *IEEE Robot. Autom. Lett.* **6**, 2405–2412 (2021).
25. H. McClintock, F. Z. Temel, N. Doshi, J.-S. Koh, R. J. Wood, The milliDelta: A high-bandwidth, high-precision, millimeter-scale Delta robot. *Sci. Robot.* **3**, eaar3018 (2018).
26. S. D. de Rivaz, B. Goldberg, N. Doshi, K. Jayaram, J. Zhou, R. J. Wood, Inverted and vertical climbing of a quadrupedal microrobot using electroadhesion. *Sci. Robot.* **3**, eaau3038 (2018).
27. H. Suzuki, R. J. Wood, Origami-inspired miniature manipulator for teleoperated microsurgery. *Nat. Mach. Intell.* **2**, 437–446 (2020).
28. J. P. Whitney, P. S. Sreetharan, K. Y. Ma, R. J. Wood, Pop-up book MEMS. *J. Micromech. Microeng.* **21**, 115021 (2011).
29. R. J. Wood, S. Avadhanula, R. Sahai, E. Steltz, R. S. Fearing, Microrobot design using fiber reinforced composites. *J. Mech. Des.* **130**, 052304 (2008).
30. M. E. Kiziroglou, B. Temelkuran, E. M. Yeatman, G.-Z. Yang, Micro motion amplification–a review. *IEEE Access* **8**, 64037–64055 (2020).
31. A. D. Horchler, A. Kandhari, K. A. Daltorio, K. C. Moses, J. C. Ryan, K. A. Stultz, E. N. Kanu, K. B. Andersen, J. A. Kershaw, R. J. Bachmann, H. J. Chiel, R. D. Quinn, Peristaltic locomotion of a modular mesh-based worm robot: Precision, compliance, and friction. *Soft Robot.* **2**, 135–145 (2015).
32. A. Kakogawa, S. Ma, A Multi-link In-pipe Inspection Robot Composed of Active and Passive Compliant Joints, in *2020 IEEE/RSJ International Conference on Intelligent Robots and Systems (IROS)* (IEEE, 2020), pp. 6472–6478.
33. A. Kakogawa, S. Ma, S. Hirose, An in-pipe robot with underactuated parallelogram crawler modules, in *2014 IEEE International Conference on Robotics and Automation (ICRA)* (IEEE, 2014), pp. 1687–1692.
34. A. Kakogawa, T. Nishimura, S. Ma, Designing arm length of a screw drive in-pipe robot for climbing vertically positioned bent pipes. *Robotica* **34**, 306–327 (2016).
35. Y.-S. Kwon, B.-J. Yi, Design and motion planning of a two-module collaborative indoor pipeline inspection robot. *IEEE Trans. Robot.* **28**, 681–696 (2012).
36. S.-g. Roh, H. R. Choi, Differential-drive in-pipe robot for moving inside urban gas pipelines. *IEEE Trans. Robot.* **21**, 1–17 (2005).
37. T. Idogaki, H. Kanayama, N. Ohya, H. Suzuki, T. Hattori, Characteristics of piezoelectric locomotive mechanism for an in-pipe micro inspection machine, in *MHS'95. Proceedings of the Sixth International Symposium on Micro Machine and Human Science* (IEEE, 1995), pp. 193–198.
38. P. Liu, Z. Wen, L. Sun, An in-pipe micro robot actuated by piezoelectric bimorphs. *Chin. Sci. Bull.* **54**, 2134–2142 (2009).
39. L. Sun, Y. Zhang, P. Sun, Z. Gong, Study on robots with PZT actuator for small pipe, in *MHS2001. Proceedings of 2001 International Symposium on Micromechatronics and Human Science (Cat. No. 01TH8583)* (IEEE, 2001), pp. 149–154.
40. J. O. Alcaide, L. Pearson, M. E. Rentschler, Design, modeling and control of a SMA-actuated biomimetic robot with novel functional skin, in *2017 IEEE International Conference on Robotics and Automation (ICRA)* (IEEE, 2017), pp. 4338–4345.
41. B. Kim, M. G. Lee, Y. P. Lee, Y. Kim, G. Lee, An earthworm-like micro robot using shape memory alloy actuator. *Sens. Actuator A-Phys.* **125**, 429–437 (2006).
42. B. Kim, S. Lee, J. H. Park, J.-O. Park, Design and fabrication of a locomotive mechanism for capsule-type endoscopes using shape memory alloys (SMAs). *IEEE-ASME Trans. Mechatron.* **10**, 77–86 (2005).
43. H. Yu, P. Ma, C. Cao, A novel in-pipe worming robot based on SMA, in *IEEE International Conference Mechatronics and Automation* (IEEE, 2005), pp. 923–927.
44. W. Adams, S. Sridar, C. M. Thalman, B. Copenhaver, H. Elsaad, P. Polygerinos, Water pipe robot utilizing soft inflatable actuators, in *2018 IEEE International Conference on Soft Robotics (RoboSoft)* (IEEE, 2018), pp. 321–326.

45. A. A. Calderón, J. C. Ugalde, J. C. Zagal, N. O. Pérez-Arancibia, Design, fabrication and control of a multi-material-multi-actuator soft robot inspired by burrowing worms, in *2016 IEEE International Conference on Robotics and Biomimetics (ROBIO)* (IEEE, 2016), pp. 31–38.
46. M. D. Gilbertson, G. McDonald, G. Korinek, J. D. Van de Ven, T. M. Kowalewski, Serially actuated locomotion for soft robots in tube-like environments. *IEEE Robot. Autom. Lett.* **2**, 1140–1147 (2017).
47. M. Ikeuchi, T. Nakamura, D. Matsubara, Development of an in-pipe inspection robot for narrow pipes and elbows using pneumatic artificial muscles, in *2012 IEEE/RSJ International Conference on Intelligent Robots and Systems* (IEEE, 2012), pp. 926–931.
48. R. Ishikawa, T. Tomita, Y. Yamada, T. Nakamura, Development of a peristaltic crawling robot for long-distance complex line sewer pipe inspections, in *2016 IEEE International Conference on Advanced Intelligent Mechatronics (AIM)* (IEEE, 2016), pp. 413–418.
49. Z. Jiao, C. Ji, J. Zou, H. Yang, M. Pan, Vacuum-powered soft pneumatic twisting actuators to empower new capabilities for soft robots. *Adv. Mater. Technol.* **4**, 1800429 (2019).
50. H. Takeshima, T. Takayama, Six-braided tube in-pipe locomotive device, in *2015 IEEE/RSJ International Conference on Intelligent Robots and Systems (IROS)* (IEEE, 2015), pp. 1125–1130.
51. M. S. Verma, A. Ainla, D. Yang, D. Harburg, G. M. Whitesides, A soft tube-climbing robot. *Soft Robot.* **5**, 133–137 (2018).
52. S. Yamazaki, Y. Tanise, Y. Yamada, T. Nakamura, Development of axial extension actuator for narrow pipe inspection endoscopic robot, in *2016 IEEE/SICE International Symposium on System Integration (SII)* (IEEE, 2016), pp. 634–639.
53. B. Zhang, Y. Fan, P. Yang, T. Cao, H. Liao, Worm-like soft robot for complicated tubular environments. *Soft Robot.* **6**, 399–413 (2019).
54. X. Zhang, T. Pan, H. L. Heung, P. W. Y. Chiu, Z. Li, A biomimetic soft robot for inspecting pipeline with significant diameter variation, in *2018 IEEE/RSJ International Conference on Intelligent Robots and Systems (IROS)* (IEEE, 2018), pp. 7486–7491.
55. Z. Zhang, X. Wang, S. Wang, D. Meng, B. Liang, Design and modeling of a parallel-pipe-crawling pneumatic soft robot. *IEEE Access* **7**, 134301–134317 (2019).
56. Q. Pei, M. Rosenthal, S. Stanford, H. Prahlad, R. Pelrine, Multiple-degrees-of-freedom electroelastomer roll actuators. *Smart Mater. Struct.* **13**, N86–N92 (2004).
57. X. Ji, X. Liu, V. Cacucciolo, Y. Civet, A. El Haitami, S. Cantin, Y. Perriard, H. Shea, Untethered feel-through haptics using 18-μm thick dielectric elastomer actuators. *Adv. Funct. Mater.* **31**, 2006639 (2021).

Acknowledgments: We thank J. Zhang, H. Sun, and R. Li for the insightful discussions. **Funding:** This work was supported by the National Natural Science Foundation of China (grant nos. 52105028, 51975306, and 92048302) and the China Postdoctoral Science Foundation (2020M680534). **Author contributions:** C.T. and H.Z. jointly conceived the pipeline inspection robot. C.T. designed and conducted all experiments, performed the collection and analysis of the experimental results, and wrote the manuscript. H.Z. analyzed the robot motion. B.D., S.J., Q.S., and X.D. assisted in the fabrication of the DEAs and simulation of the anchoring unit. X.-J.L. and H.Z. reviewed and edited the manuscript. **Competing interests:** C.T., B.D., S.J., X.-J.L., and H.Z. applied for two patents related to this work in China (nos. 202111115113.2 and 202111116932.9). The other authors declare that they have no competing interests. **Data and materials availability:** All data needed to evaluate the conclusions in the paper are present in the paper or the Supplementary Materials. The MATLAB code for analyzing the robot motion is available at https://cloud.tsinghua.edu.cn/f/2624899028ea404abda5/?dl=1.

Submitted 27 October 2021
Accepted 3 May 2022
Published 25 May 2022
10.1126/scirobotics.abm8597

Science Robotics

A pipeline inspection robot for navigating tubular environments in the sub-centimeter scale

Chao Tang, Boyuan Du, Songwen Jiang, Qi Shao, Xuguang Dong, Xin-Jun Liu, and Huichan Zhao

Sci. Robot. **7** (66), eabm8597. DOI: 10.1126/scirobotics.abm8597

Science Robotics (ISSN 2470-9476) is published by the American Association for the Advancement of Science. 1200 New York Avenue NW, Washington, DC 20005. The title *Science Robotics* is a registered trademark of AAAS.